


Cite this: *RSC Adv.*, 2021, 11, 3333

Highly efficient $\text{In}_2\text{S}_3/\text{WO}_3$ photocatalysts: Z-scheme photocatalytic mechanism for enhanced photocatalytic water pollutant degradation under visible light irradiation†

Qingqing Qiu,^a Peng Zhu,^a Yao Liu,^b Tongxiang Liang,^a Tengfeng Xie^{*c} and Yanhong Lin^c

A Z-scheme system $\text{In}_2\text{S}_3/\text{WO}_3$ heterojunction was fabricated *via* a mild hydrothermal method and further applied for photocatalytic degradation of tetracycline (TCH) and Rhodamine B (Rh B) under visible light irradiation. The morphological structure, chemical composition and optical properties were studied by XRD, SEM, HRTEM and UV-visible absorption spectra. The results revealed that $\text{In}_2\text{S}_3/\text{WO}_3$ hierarchical structures were successfully constructed, and the prepared $\text{In}_2\text{S}_3/\text{WO}_3$ photocatalysts exhibited enhanced visible-light absorption compared to pure WO_3 nanorods, which are essential to improve the photocatalytic performance. The degradation rate of TCH using the $\text{In}_2\text{S}_3(40 \text{ wt}\%)/\text{WO}_3$ heterostructure (WI40) photocatalyst was about 212 times and 22 times as high as that for pure WO_3 and pure In_2S_3 , respectively. The degradation rate of Rh B with the WI40 photocatalyst was about 56 times the efficiency of pure WO_3 and 7.6 times that of pure In_2S_3 . The results of the surface photovoltage (SPV), transient photovoltage (TPV) and reactive oxidation species (ROS) scavenger experiments indicated that the Z-scheme system of $\text{In}_2\text{S}_3/\text{WO}_3$ is favorable for photoexcited charge transfer at the contact interface of In_2S_3 and WO_3 , which benefits the charge separation efficiency and depresses the recombination of photoexcited charge, resulting in favorable photocatalytic pollutant degradation efficiency under visible light irradiation.

Received 2nd November 2020
Accepted 26th December 2020

DOI: 10.1039/d0ra09315g

rsc.li/rsc-advances

1 Introduction

In the past few decades, water pollutants have seriously threatened human health due to rapidly developing industries.^{1–5} Various techniques for purifying the environment have been investigated. Among these techniques, photocatalytic degradation technology has captured much attention as a new environment-purifying technique because of its low toxicity, low cost and easy recovery.^{6–8} However, the performance of most photocatalysts is seriously restricted by the range of sunlight utilization and the photoexcited charge separation efficiency.⁹

Recent studies suggest that an excellent catalytic system should meet three conditions: the high utilization of sunlight, strong oxidation–reduction properties and high separation efficiency of photoexcited charge.^{10–13} Obviously, it is difficult to have high catalytic activity for a mono-component

semiconductor photocatalyst. In this regard, construction of heterojunction structures is an effective method to boost the photocatalytic performance.¹⁴ The traditional type II heterojunction structures can achieve a band structure with adjustable and high separation efficiency of photogenerated charge.¹⁵ However, the type II heterojunction structures lead to photoexcited electron transfer to the conduction band with lower position, then the photoexcited holes transfer to the valence band with a higher position, which is a disadvantage for the photocatalytic oxidation–reduction properties of photoexcited charge.^{10,15} Thus, the design and construction of novel heterojunction structures seem inevitable. The design of Z-scheme heterojunction structures instantly became the focus of photocatalytic studies, and is considered to be the most promising strategy to solve the issues above.^{15,16}

To date, many studies about Z-scheme heterojunction structures have been reported, such as $\text{g-C}_3\text{N}_4/\text{WO}_3$, $\text{CdS}/\text{Au}/\text{TO}_2$, $\text{CdS}/\text{Au}/\text{WO}_3$, $\text{Mn}_x\text{Cd}_{1-x}\text{S}/\text{WO}_3$, $\text{ZnO}/\text{Au}/\text{SnO}_2$, $\text{CeO}_2/\text{Ag}/\text{AgBr}$, $\text{WO}_3/\text{Au}/\text{In}_2\text{S}_3$, $\text{CdS}/\text{Au}/\text{BiVO}_4$ and $\text{BiOI}/\text{Pt}/\text{g-C}_3\text{N}_4$.^{17–25} In most cases of the Z-scheme heterojunction catalytic system, however, noble metals are used as the electron mediator, such as Pt, Au and Ag, which can increase the cost of preparation and application.²⁶ Thus, it is necessary to construct direct Z-scheme heterojunction structures.

^aCollege of Rare Earths, Jiangxi University of Science and Technology, Ganzhou 341000, P. R. China

^bFaculty of Materials Metallurgy and Chemistry, Jiangxi University of Science and Technology, Ganzhou 341000, P. R. China

^cCollege of Chemistry, Jilin University, Changchun 130012, P. R. China

† Electronic supplementary information (ESI) available. See DOI: 10.1039/d0ra09315g



Indium sulfide (In_2S_3), with a bandgap of 2.2 eV, is an effective visible-light-driven photocatalyst that has been extensively used in the field of photocatalysis due to its narrow bandgap, good chemical stability and low toxicity.^{27–30} Besides these, the energy structure of In_2S_3 semiconductor has excellent reduction performance due to its conduction band with a higher position. But the In_2S_3 crystal has poor crystallinity and too rapid rate of charge recombination, which leads to undesirable photocatalytic degradation activity.^{29,30} WO_3 semiconductor has high carrier mobility, good crystallinity, good chemical stability, thermal stability and excellent antioxidant properties due to its valence band with lower position compared to other semiconductor materials, but has a wide bandgap and the limitation of visible-light utilization.^{31–33} Thus, we exploit a suitable preparation method to prepare $\text{In}_2\text{S}_3/\text{WO}_3$ composite, which can expand visible light utilization and improve the photoexcited charge separation efficiency. Besides, we also noticed that the Z-scheme system $\text{WO}_3/\text{Au}/\text{In}_2\text{S}_3$ was used in the photocatalytic reduction of CO_2 .²⁴ The report suggested that the Z-scheme $\text{In}_2\text{S}_3/\text{WO}_3$ heterostructure can form and accelerate the rate of charge carrier separation. However, there are few reports on the application and photocatalytic mechanism of all-solid-state Z-scheme $\text{In}_2\text{S}_3/\text{WO}_3$ heterostructure in photocatalytic degradation.

Based on the above discussion, we focus on the construction of a direct Z-scheme $\text{In}_2\text{S}_3/\text{WO}_3$ heterostructure through a simple and facile method. The degradation efficiency of the all-solid-state $\text{In}_2\text{S}_3/\text{WO}_3$ photocatalyst was much higher than that of the pristine In_2S_3 and WO_3 . The photoexcited charge behavior of the Z-scheme $\text{In}_2\text{S}_3/\text{WO}_3$ heterostructure was studied using the SPV and TPV techniques. Furthermore, reactive oxidation species (ROS) scavenger experiments confirmed that the Z-scheme $\text{In}_2\text{S}_3/\text{WO}_3$ structure induces electrons in In_2S_3 and holes in WO_3 with an unobstructed charge transfer route, effectively improving the separation efficiency of photoexcited charge.

2 Experimental details

2.1. Preparation of WO_3 nanorods

The WO_3 nanorods were prepared using a simple hydrothermal method according to the previous reports.^{26,31} In a typical experiment, 2.0 g of sodium tungstate hydrate and 0.6 g of sodium chloride in 60 mL distilled water was stirred for 6 h at room temperature. Afterwards, concentrated hydrochloric acid was added dropwise until the pH of solution reached 2.0, and the solution was kept stirring for 3 h. The resulting solution was transferred to a 100 mL Teflon-lined stainless steel autoclave and heated at 180 °C for 24 h. Finally, the obtained WO_3 nanorods were centrifuged and washed with distilled water and ethanol, and then the precipitates were dried at 50 °C for 12 h under vacuum condition.

2.2. Preparation of the Z-scheme $\text{In}_2\text{S}_3/\text{WO}_3$ photocatalyst

The Z-scheme $\text{In}_2\text{S}_3/\text{WO}_3$ photocatalyst was prepared by a simple and facile hydrothermal method. First, 0.3 g of WO_3

was ultrasonically dispersed in 30 mL distilled water. A certain amount of indium trichloride hydrate was dissolved in the WO_3 suspension, then a certain amount of sodium sulfide hydrate was added dropwise. After vigorous stirring for 5 h, the mixture was transferred to a 100 mL Teflon-lined stainless steel autoclave and heated at 180 °C for 12 h. Finally, the obtained precipitate was centrifuged and washed with distilled water and ethanol, and the precipitates were dried at 50 °C for 12 h under vacuum condition. The mass ratios of In_2S_3 to WO_3 were $R = 0, 20, 30, 40$ and 50 , which were marked as W10, W120, W130, W140 and W150, respectively. The pure In_2S_3 powder sample was prepared under the same conditions without WO_3 powder.

2.3. Characterization and measurements

The surface morphology of the obtained powder samples was examined by the MLA 650F field emission scanning electron microscope (SEM, Navo NanoSEM FEI). X-ray diffraction (XRD) was carried out to study the crystal structure of the samples using an X-ray diffractometer with Cu K α radiation (Empyrean, PANalytical B.V.; $\lambda = 1.54 \text{ \AA}$) in the range of 10–70° (2 θ). The absorption spectra were measured with a UV-vis spectrophotometer (UV3600, Shimadzu).

Surface photovoltage (SPV) spectra were obtained using a lock-in-based surface photovoltage (SPV) measurement system with a grating monochromator (Omni- λ 5007, Zolix), a lock-in amplifier (model SR830-DSP), and an optical chopper (model SR540) running at a frequency of 24 Hz.³⁴ Transient photovoltage (TPV) measurements were carried out using a self-assembled instrument with a Nd:YAG laser (Q-smart 450, Quantl, Inc.).^{34,35} The intensity of the pulse was regulated with a neutral gray filter and a Joule meter (Starlite, Ophir, Inc.). The transient signal was recorded using a 500 MHz digital phosphor oscilloscope (TDS 5054, Tektronix). Both the SPV and TPV measurements were performed in ambient air.

2.4. Photocatalytic degradation experiments

In a typical photocatalytic degradation experiment, 50 mg of photocatalyst was mixed with 100 mL of tetracycline hydrochloride aqueous solution (TCH, 30 mg L^{−1}) (pH = 4.5) or Rhodamine B aqueous solution (Rh B, 35 mg L^{−1}) (pH = 6.0), then ultrasonically dispersed for 5 min. The obtained mixed solution was vigorously stirred for 30 min in the dark to achieve the absorption-desorption equilibrium. In order to investigate the water pollutant degradation efficiency, 1 mL of the mixture was taken out after a given time interval and centrifuged for 10 min to achieve the purpose of solid-liquid separation after visible light irradiation ($\lambda > 420 \text{ nm}$). The concentration of TCH and Rh B was measured with the absorption wavelength of 357 nm and 554 nm, respectively, using a UV-vis spectrometer (UV 2400).

Scavenger tests for reactive oxidation species (ROSS) were carried out under the same experimental conditions except for the addition of scavengers for the degradation process. Potassium bromate (KBrO_3 , 10 mM), sodium oxalate ($\text{Na}_2\text{C}_2\text{O}_4$, 10 mM), 2,2,6,6-tetramethylpiperidine-1-oxyl (TEMPOL, 10 mM) and isopropanol (10 mM) were used as e^- , h^+ , 'O_2^- and 'OH scavengers, respectively.



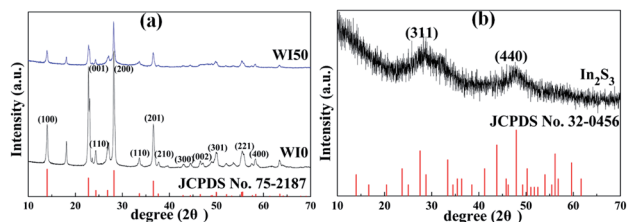


Fig. 1 XRD patterns of (a) W10, W150 and (b) In_2S_3 .

3 Results and discussion

3.1. Structural characterization of photocatalysts

Fig. 1 shows the X-ray diffraction (XRD) patterns of W10, W150 and In_2S_3 samples. The crystal structure of pure WO_3 is hexagonal phase (JCPDS card no. 75-2187), as shown in Fig. 1(a).^{26–31} The crystal structure of pure In_2S_3 is cubic phase (JCPDS card no. 32-0456), as shown in Fig. 1(b).^{7,28} Fig. 1(a) shows that only the hexagonal structure WO_3 is observed, and no obvious diffraction peak is observed for the W150 sample. This may be attributed to the diffraction peak of In_2S_3 sample being too weak compared to the diffraction peak of WO_3 . In addition, the intensity of diffraction peak for the W120, W130, W140 and W150 samples is weakened compared to that for the pure WO_3 , which shows that the preparation of $\text{In}_2\text{S}_3/\text{WO}_3$ composites makes the crystallinity poorer (see Fig. S1†). With the increase of In_2S_3 loading, the intensity of diffraction peak becomes slightly weaker due to the reduced WO_3 content.

The morphology of pure WO_3 , In_2S_3 , In_2S_3 (20 wt%)/ WO_3 and In_2S_3 (40 wt%)/ WO_3 samples was determined by FESEM (Fig. 2). It can be seen from Fig. 2(a) that the pure WO_3 consists of nanorods and bulk nanomaterials. The length of nanomaterials is about 0.1–1.1 μm , and the width is about 100–350 nm. Tiny

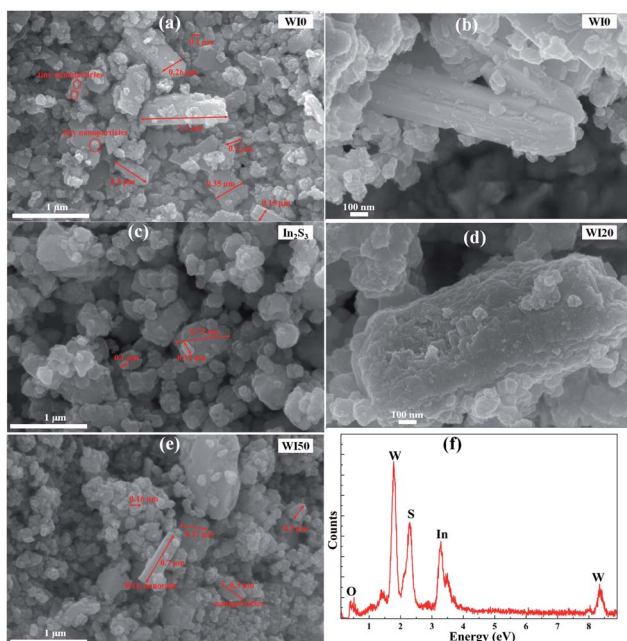


Fig. 2 FESEM images of (a and b) W10, (c) In_2S_3 , (d) W120, (e) W150; (f) energy-dispersive X-ray spectroscopy (EDX) of W140.

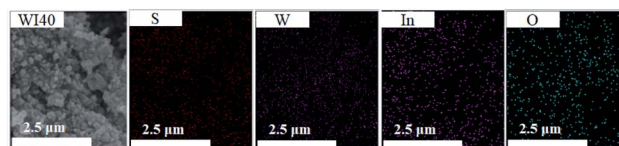


Fig. 3 EDX mappings of W140.

nanoparticles with diameters of 10–110 nm can be observed on the surface of nanorods and bulk nanomaterials. The surface of the nanorods is smooth for pure WO_3 (see Fig. 2(b)). As shown in Fig. 2(c), In_2S_3 nanoparticles with diameters of 100–720 nm were obtained. However, the surface of the nanorods becomes rough with the loading of In_2S_3 (see Fig. 2(d)). Fig. 2(e) shows that the nanoparticles increase significantly for W140 composite, which proves that the In_2S_3 nanoparticles are loaded on the WO_3 nanorods and bulk nanomaterials. In Fig. 2(f), the EDX of W140 illustrates that the W140 composite consists of O, W, S and In atoms. Therefore, the above analyses indicate the In_2S_3 is deposited on the WO_3 successfully. The EDX mapping images obtained using TEM-EDX spectroscopy are shown in Fig. S2, S3† and 3. Fig. S2 and S3† show that only the elements W and O for pure WO_3 , and the elements In and S for pure In_2S_3 are detected. Fig. 3 shows the presence of W, O, In and S for W140. The results illustrate all the elements are well distributed.

Fig. 4 shows the transition electron microscopy (TEM) and high-magnification transition electron microscopy (HRTEM) images of WO_3 , In_2S_3 and W140. Fig. 4(a) shows that the pure WO_3 is made up of nanorods, bulk nanomaterials and tiny

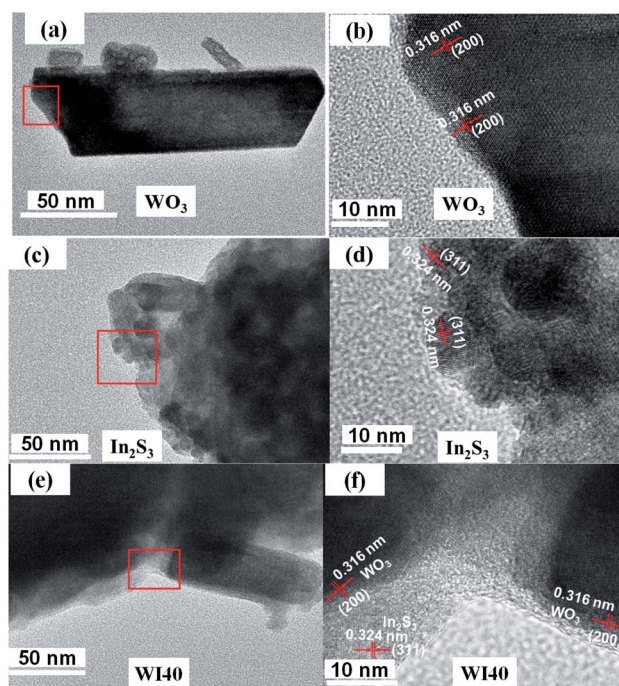


Fig. 4 (a) TEM image of WO_3 and (b) HRTEM image of WO_3 ; (c) TEM image of In_2S_3 and (d) HRTEM image of In_2S_3 ; (e) TEM image of W140 and (f) HRTEM image of WO_3 and In_2S_3 .

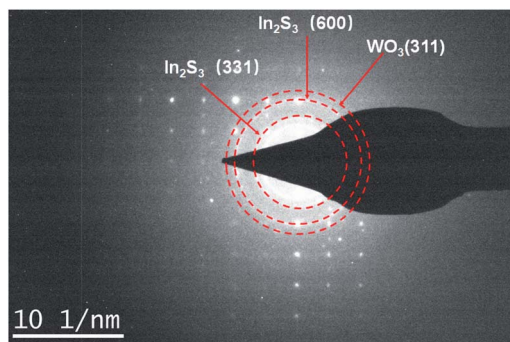


Fig. 5 SAED pattern of WI40.

nanoparticles, corresponding to the SEM images of WO_3 . The lattice spacing of WO_3 in the (200) plane is 0.316 nm (see Fig. 4(b)). Fig. 4(c) shows that pure In_2S_3 is made up of nanoparticles, and the lattice spacing of In_2S_3 in the (311) plane is 0.324 nm (see Fig. 4(d)). As shown in Fig. 4(e), the In_2S_3 nanoparticles closely connect with WO_3 nanomaterials. The HRTEM in Fig. 4(f) shows the $\text{In}_2\text{S}_3/\text{WO}_3$ heterojunction is formed between In_2S_3 and WO_3 . One can see in Fig. 4(f) that the lattice spacing of 0.316 nm is ascribed to the (200) plane of WO_3 , while the lattice spacing of 0.324 nm is ascribed to the (211) plane of In_2S_3 . The results confirm that WO_3 and In_2S_3 are in close contact with each other, clearly indicating growth of the $\text{In}_2\text{S}_3/\text{WO}_3$ hierarchical structures.

In addition, we then performed the selected area electron diffraction (SAED) pattern of WI40 to examine the $\text{In}_2\text{S}_3/\text{WO}_3$ hierarchical structures for more detailed information. Fig. 5 indicates that the lattice spacing of 0.247 nm and 0.179 nm correspond to the values of the (311) lattice plane of hexagonal phase WO_3 (JCPDS card no. 75-2187), and the observed 0.247 nm and 0.179 nm lattice spacing can be assigned to the (600) and (311) planes of cubic phase In_2S_3 (JCPDS card no. 32-0456). The results further indicate that the $\text{In}_2\text{S}_3/\text{WO}_3$ hierarchical structures were successfully constructed.

The absorption spectra of WI0, WI40 and In_2S_3 samples are shown in Fig. 6. The absorption band edge of pure WO_3 is about 435 nm, and that of pure In_2S_3 is about 540 nm. In addition, the absorption band edge of $\text{In}_2\text{S}_3/\text{WO}_3$ composites exhibits a red shift with the increase of In_2S_3 loading. The bandgap energy of the semiconductor is calculated by the following formula:³¹

$$(\alpha h\nu) = A(h\nu - E_g)^{n/2},$$

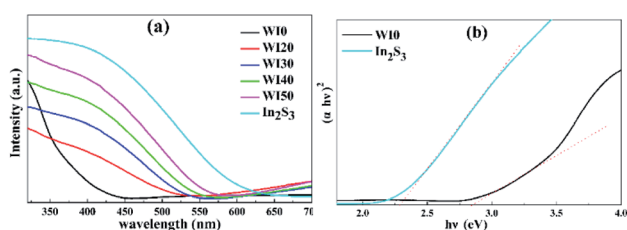


Fig. 6 (a) UV-visible absorption spectra of WI0, WI20, WI30, WI40, WI50 and In_2S_3 . (b) Plots of the $(\alpha h\nu)^2$ versus photon energy ($h\nu$) for In_2S_3 and WI0.

where ν , α , A , and E_g are light frequency, absorption index, constant value, and bandgap energy of the semiconductor, respectively.^{28,31} In addition, the value of n depends on the transition type of the semiconductor ($n = 1$ for direct transition semiconductor, $n = 4$ for indirect transition semiconductor). The values of n for In_2S_3 and WO_3 are 1 and 4, respectively.^{28,31} As shown in Fig. 6(b), the E_g of WO_3 is calculated to be 2.85 eV, and the E_g of In_2S_3 is about 2.3 eV. With the increase of In_2S_3 loading, the E_g of $\text{In}_2\text{S}_3/\text{WO}_3$ composites is closer to that of In_2S_3 , which indicates the loading of In_2S_3 leads to the improvement of visible light utilization.

3.2. Photocatalytic performance of photocatalysts

The degradation of Rhodamine B (Rh B) under visible light irradiation ($\lambda > 420$ nm) was investigated in order to estimate the photocatalytic performance of the prepared photocatalysts. As shown in Fig. 7(a), the Rh B degradation efficiency of 11% was obtained for pure WO_3 after 20 min of irradiation with visible light, and the Rh B degradation efficiency of 56.54% was obtained for pure In_2S_3 under the same condition. However, Fig. 7(a) shows that the $\text{In}_2\text{S}_3/\text{WO}_3$ composites display apparently superior Rh B degradation activity. The degradation efficiencies of Rh B are 82.2%, 96.0%, 97.8%, and 96.9% for WI20, WI30, WI40, and WI50 composites, respectively, after 20 min of irradiation. Fig. S4(a)† shows the UV-visible absorption spectra of Rh B solutions before and after photocatalytic degradation reaction in the presence of WI40. The WI40 photocatalyst shows an obvious and significant degradation effect, and Rh B is almost completely degraded after 20 min of irradiation with visible light.

In order to quantitatively evaluate the reaction kinetics of Rh B degradation, the experimental data in Fig. 7(a) could be fitted by the Langmuir–Hinshelwood model and expressed by the following equation:³⁶

$$\ln(C_0/C) = k_{\text{app}}t,$$

where C_0 and C are the concentrations of Rh B at irradiation time of t_0 and t , respectively, and k_{app} is the pseudo-first-order rate constant of Rh B photodegradation (min^{-1}). According to the experimental data in Fig. 7(a), the linear fitting curves of $\ln(C_0/C)$ versus irradiation time t was obtained, as shown in Fig. 7(b). The Rh B degradation rate constant k was calculated to

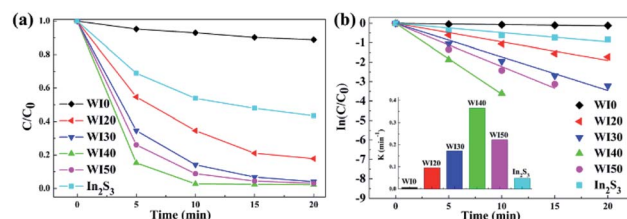


Fig. 7 (a) Photocatalytic degradation performance of WI0, WI20, WI30, WI40, WI50 and In_2S_3 for Rh B under visible light irradiation; (b) corresponding plots of $\ln(C_0/C)$ versus irradiation time t and the calculated rate constant k .



Table 1 Comparison of Rh B photocatalytic activity with other photocatalysts

| Catalyst | Rh B Concentration (mg L ⁻¹) | Catalyst Concentration (g L ⁻¹) | <i>k</i> (min ⁻¹) | Reference |
|--|--|---|-------------------------------|-----------|
| In ₂ S ₃ /WO ₃ | 35 | 0.50 | 0.365 | This work |
| Mn ₃ O ₄ /CeO ₂ | 10 | 0.67 | 0.015 | 39 |
| Carbon/g-C ₃ N ₄ | 5 | 0.05 | 0.008 | 40 |
| TiO ₂ /C | 5 | 0.1 | 0.080 | 41 |
| C ₃ N ₄ /B-C-dots | 10 | 0.5 | 0.036 | 42 |
| WO ₃ /Cu(II) | 10 | 0.33 | 0.010 | 43 |

be 0.0065, 0.0953, 0.1728, 0.3646, 0.2226 and 0.0477 min⁻¹ for WI0, WI20, WI30, WI40, WI50 and In₂S₃. The results illustrate that the maximum Rh B degradation rate (0.3646 min⁻¹) was acquired using the WI40 composites, 56 times as high as pure WO₃ and 7.6 times as high as pure In₂S₃ when exposed to 20 min of visible light. This may be attributed to the synergistic reaction of WO₃ and In₂S₃ in the all-solid-state composite photocatalyst, and the interaction is beneficial to the improvement of photocatalytic degradation efficiency. Yet as the amount for In₂S₃ loading continuously increases, the degradation efficiency of WI50 exhibits a slight decrease compared to that of WI40, and two reasons could explain this decrease of degradation efficiency. On the one hand, the high content of In₂S₃ could block the WO₃ from absorbing light, which is unfavorable for the interaction between WO₃ and In₂S₃. On the other hand, the excess amount of In₂S₃ can serve as the recombination center of photoexcited charges, which would decrease the activity of the composite photocatalyst.^{37,38} Furthermore, the WI40 also exhibits outstanding photocatalytic performance for Rh B degradation compared with the latest works (Table 1).

The degradation efficiency of tetracycline hydrochloride (TCH) under visible light irradiation was studied to further investigate the effect of the interaction between WO₃ and In₂S₃. As shown in Fig. 8(a), the degradation efficiencies of TCH for pure WO₃ and In₂S₃ are 7.1% and 56.6%, respectively, after 150 min of irradiation. However, the degradation efficiencies of TCH are 51.6%, 62.5%, 84.7%, and 81.4% for WI20, WI30, WI40, and WI50 composites after 150 min of irradiation. The corresponding curves of ln(C₀/C) versus irradiation time *t* and the degradation rate constant *k* were also calculated, as shown in Fig. 8(b). The degradation rate constants (*k*) of TCH are

0.0004, 0.0036, 0.0039, 0.0085, 0.0074 and 0.0038 min⁻¹ for WI0, WI20, WI30, WI40, WI50 and In₂S₃, respectively. The TCH degradation rate constants for WI40 are about 212 times and 22 times as high as that for pure WO₃ and pure In₂S₃, respectively, illustrating that the WI40 composite photocatalyst is apparently superior to pure WO₃ and In₂S₃. Moreover, the UV-visible absorption spectra of TCH solutions before and after photocatalytic degradation reaction in the presence of WI40 was recorded, as shown in Fig. S4(b).† Significantly, the WI40 photocatalyst exhibits effective degradation of the TCH pollutant, and the degradation efficiency for TCH is close to 90% under visible light irradiation. However, WI40 shows relatively low photocatalytic performance for TCH degradation compared with the latest works (Table 2), which suggests that the prepared photocatalyst is more suitable for Rh B degradation. The above results indicate that the synergistic effect between WO₃ and In₂S₃ plays a crucial role for the degradation of these water pollutants.

The degradation of Rh B and TCH might be affected under different solution pH conditions.¹⁷ The degradation experiments were carried out at different pH values, as shown in Fig. S5.† The result indicates that the alkaline solution has remarkable impact on the degradation efficiency of Rh B, where neutral and acidic solutions only have a mild effect on the degradation efficiency; 97.89%, 96.79%, 98.23% and 90.57% of Rh B were removed at pH values of 2, 4, 7 and 10, respectively. However, the initial pH only has slight impact on the photocatalytic activity for TCH degradation, and 82.28%, 84.94%, 86.47% and 85.23% of TCH were removed at pH values of 2, 5, 7 and 9. This gives evidence that the In₂S₃/WO₃ photocatalyst maintains a relatively high photocatalytic performance over a wide pH range. To investigate further, a physical mixture of pure WO₃ and In₂S₃ with the same mass ratio (40%) was used as the control during photocatalytic degradation, as shown in Fig. S6.† Obviously, the degradation performance of WI40 is better, compared to that of the physical mixture of In₂S₃(40 wt%)/WO₃ for Rh B and TCH degradation under visible light irradiation.

Stability tests of the WI40 photocatalyst for photocatalytic degradation of Rh B and TCH were conducted, as illustrated in Fig. 9. The Rh B degradation efficiency varies from 97.8 to 98.9% after 20 min of irradiation with visible light, and the TCH degradation efficiency varies from 84.7 to 87.9% after 150 min of irradiation under the same condition. There is no significant decline of photocatalytic degradation activity toward Rh B and TCH after four cycles, indicating that the WI40 photocatalyst

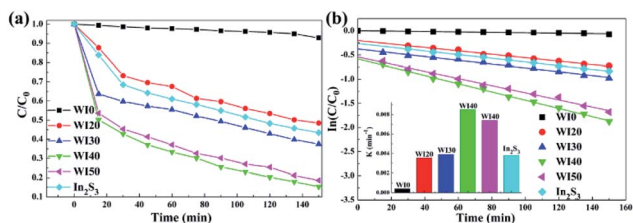


Fig. 8 (a) Photocatalytic degradation performance of WI0, WI20, WI30, WI40, WI50 and In₂S₃ for TCH under visible light irradiation; (b) corresponding plots of ln(C₀/C) versus irradiation time *t* and the calculated rate constant *k*.



Table 2 Comparison of TCH photocatalytic activity with other photocatalysts

| Catalyst | TCH concentration (mg L ⁻¹) | Catalyst concentration (g L ⁻¹) | <i>k</i> (min ⁻¹) | Reference |
|---|---|---|-------------------------------|-----------|
| In ₂ S ₃ /WO ₃ | 30 | 0.5 | 0.009 | This work |
| C ₃ N ₄ /B-C-dots | 10 | 0.5 | 0.023 | 42 |
| Ag ₂ CO ₃ /Ag/WO ₃ | 10 | 0.5 | 0.018 | 44 |
| Ag ₃ PO ₄ /BiVO ₄ | 5 | 0.5 | 0.013 | 45 |
| BiOBr/Ag ₃ PO ₄ | 20 | 0.5 | 0.078 | 46 |
| TiO ₂ /CdS | 50 | 0.6 | 0.030 | 47 |

has good stability. Moreover, the physical structure of the fresh and recycled In₂S₃/WO₃ composites was characterized by XRD technique (Fig. S7†). No obvious changes can be observed between the fresh and recycled photocatalyst. The results further confirm that the prepared In₂S₃/WO₃ photocatalyst has outstanding stability after repeated recycling.

3.3. Assessment of the separation efficiency of photoexcited charge carriers

SPV technique was employed to explore the process of photoexcited charge carrier separation and transport in the surface and interface of the photocatalyst samples. The schematic diagram of the SPV test configuration is shown in Fig. 10. For the pure WO₃, the SPV response is at the wavelength of 300–450 nm, which corresponds to the band-to-band transitions of WO₃. For the pure In₂S₃, the SPV response is around the wavelength of 300–620 nm, which corresponds to the band-to-band transitions of In₂S₃. However, the SPV response of WI40 expands to about 620 nm due to the loading of In₂S₃, and the SPV intensity of WI40 is significantly stronger compared to that of pure WO₃ and In₂S₃. It is generally accepted that for a similar composition of semiconductors, the higher the SPV response intensity, the higher the separation efficiency of the photoexcited charge, indicating interfacial interaction in the all-solid-state composite photocatalyst is in favor of the separation and transport of photoexcited charge carriers and photocatalytic degradation efficiency.⁴⁸ This is credible evidence for the crucial role of the construction of the Z-scheme In₂S₃/WO₃ heterostructure.^{25,31}

Furthermore, the transient photovoltage (TPV) technique was applied to investigate the dynamic properties of the photoexcited charge separation and transfer process of WI0, WI40 and In₂S₃. Fig. 11 illustrates the TPV results of prepared photocatalysts under 355 nm and 532 nm pulse laser irradiation on a normal timescale. The schematic diagram of the TPV test configuration is presented as well as that of the SPV test configuration, as seen in the inset of Fig. 10. Obviously, a negative TPV signal is observed for all the prepared photocatalysts, which implies the photoexcited electrons transfer to the top electrode. Moreover, a weak positive TPV signal is observed for all the prepared photocatalysts due to the existence of surface state.^{49,50} As shown in Fig. 11(a), only a weak signal is observed for the pure WO₃ and In₂S₃ due to the poor separation efficiency of the pure WO₃ and In₂S₃. Similarly, the TPV response intensity of WI40 is significantly stronger compared to that of pure WO₃ and In₂S₃, which reveals that the synergistic reaction of WO₃ and In₂S₃ is beneficial to the separation and transport of photoexcited charge carriers. The TPV response of the prepared photocatalysts shows the same results under 532 nm pulse laser irradiation, as shown in Fig. 11(b). That is to say, WI40 shows a higher photocatalytic water pollutant degradation efficiency, which is reasonable due to the synergistic reaction of WO₃ and In₂S₃.

3.4. Exploration of photocatalytic degradation mechanism

In order to further understand the photocatalytic degradation mechanism of In₂S₃/WO₃ heterostructure, scavenger experiments for WI0 (Fig. 12(a)) and WI40 (Fig. 12(b)) were carried out

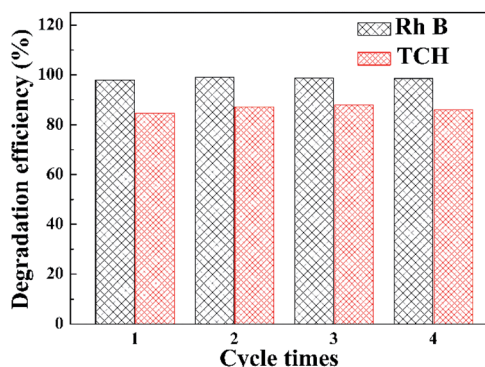


Fig. 9 Stability testing of the WI40 photocatalyst toward the photocatalytic degradation of Rh B and TCH under visible light irradiation.

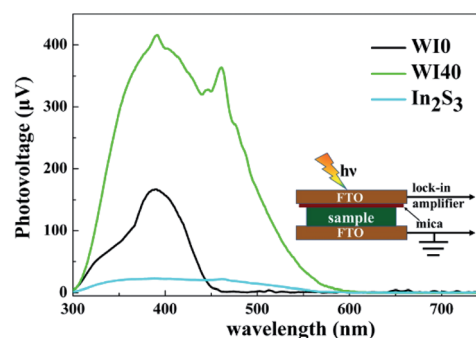


Fig. 10 Surface photovoltage spectra of WI0, WI40 and In₂S₃.



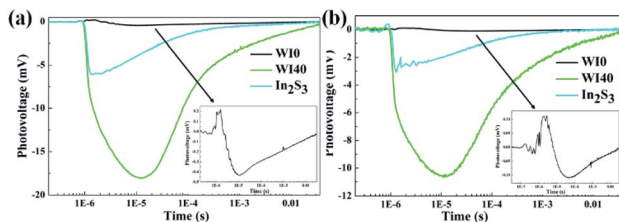


Fig. 11 Transient photovoltage response of W10, WI40 and In_2S_3 . (a) The wavelength and the intensity of the laser are 355 nm and 100 μJ , respectively. (b) The wavelength and the intensity of the laser are 532 nm and 100 μJ , respectively.

to investigate the reactive oxidation species (ROSs) in the degradation process. It is worth noting that the degradation efficiencies decrease obviously both in the presence of potassium bromate and sodium oxalate in the W10 photocatalytic degradation system, indicating that e^- and h^+ are the main ROS in the degradation process of W10, while $\cdot\text{O}_2^-$ and $\cdot\text{OH}$ rarely exist. In contrast, all four types of ROS exist in the WI40 photocatalytic degradation system. The degradation efficiency decreases sharply in the presence of TEMPOL, indicating that $\cdot\text{O}_2^-$ is the major ROS in the degradation process of WI40. However, the degradation efficiencies decrease weakly both in the presence of potassium bromate and isopropanol, which means that h^+ and $\cdot\text{OH}$ are the minor ROS. Besides, the degradation efficiency decreases with the addition of sodium oxalate, indicating that holes also take part in the oxidation reaction of pollutants. It should be noted that the concentration of e^- and h^+ reduce sharply in the WI40 system; this may be due to the fact that the photoexcited charges transfer rapidly to form $\cdot\text{O}_2^-$ and $\cdot\text{OH}$. In fact, previous reports suggest that the CB position of In_2S_3 is at around -0.7 eV,²³ and the redox potential of $\text{O}_2/\cdot\text{O}_2^-$ (-0.33 eV vs. NHE) is more negative than the CB of the In_2S_3 ; thus, the electrons in the CB of In_2S_3 could react with O_2 to produce $\cdot\text{O}_2^-$. This is consistent with the results of the scavenger experiments. Similarly, the VB position of WO_3 (3.2 eV vs. NHE) is more positive than the redox potential of $\cdot\text{OH}/\text{OH}^-$ (2.4 eV vs. NHE), and $\cdot\text{OH}$ could be generated through the reaction between holes in the VB and OH^- .^{25,26} Therefore, the all-solid-state Z-scheme $\text{In}_2\text{S}_3/\text{WO}_3$ heterostructure is proposed.

Based on the above analysis of experimental results, the possible photocatalytic degradation mechanism with the all-solid-state Z-scheme $\text{In}_2\text{S}_3/\text{WO}_3$ heterostructure is shown in Fig. 13. Previous reports confirmed that the energy band

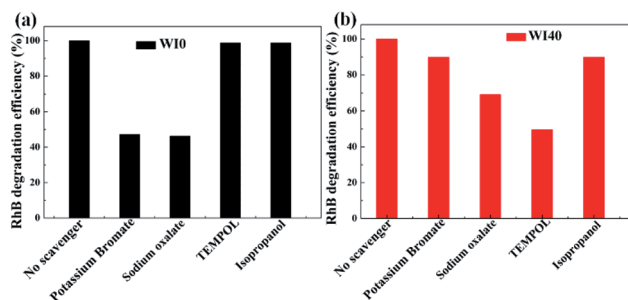


Fig. 12 ROS scavenger experiments during the photodegradation of Rh B over (a) W10 and (b) WI40 under visible light irradiation.

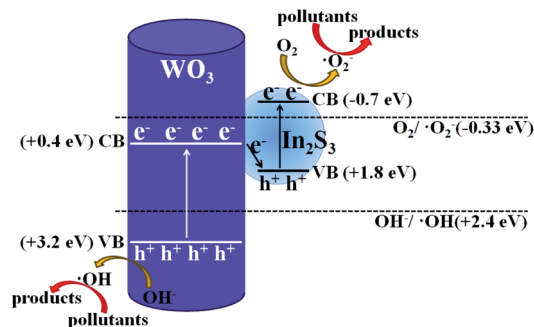


Fig. 13 Possible photocatalytic pollutant degradation mechanism for the all-solid-state Z-scheme $\text{In}_2\text{S}_3/\text{WO}_3$ photocatalyst.

structures of WO_3 and In_2S_3 are beneficial to the transfer of photoexcited electrons from the CB of WO_3 to the VB of In_2S_3 .²³ Therefore, the charge recombination of electrons in WO_3 and holes in In_2S_3 occurs at the contact interface between WO_3 and In_2S_3 ; this leaves the electrons in the CB of In_2S_3 and holes in the VB of WO_3 to take part in the photocatalytic degradation reaction directly, or generate the $\cdot\text{O}_2^-$ and $\cdot\text{OH}$. In this way, the $\cdot\text{O}_2^-$ with stronger oxidation ability will participate in the oxidation reaction of pollutants and improve the photocatalytic degradation efficiency, as shown in Fig. 13. The above discussion confirms that the designed all-solid-state Z-scheme photocatalyst could promote photocatalytic water pollutant degradation efficiency and enhance the redox ability of the photocatalytic system distinctly.

4 Conclusions

In summary, an all-solid-state Z-scheme $\text{In}_2\text{S}_3/\text{WO}_3$ photocatalyst was successfully designed and synthesized *via* a facile method. The degradation efficiency of the $\text{In}_2\text{S}_3/\text{WO}_3$ photocatalyst exhibits a significant improvement compared with the pure In_2S_3 and WO_3 . The results suggest that the all-solid-state Z-scheme $\text{In}_2\text{S}_3/\text{WO}_3$ heterostructure is more beneficial to the photoexcited charge transfer at the contact interface with an unobstructed Z-scheme route, and thus the separation efficiency shows a clear improvement. In this way, the obtained $\text{In}_2\text{S}_3/\text{WO}_3$ photocatalyst exhibits a significantly improved photocatalytic degradation performance toward Rh B and TCH, eventually. This work demonstrates that the all-solid-state Z-scheme photocatalyst could be accurately designed and prepared *via* a simple hydrothermal method, and it exhibits outstanding photocatalytic performance, presenting a novel route for the design of a highly efficient photocatalyst in the photocatalytic field.

Conflicts of interest

There are no conflicts to declare.

Acknowledgements

We are grateful to the National Natural Science Foundation of China (No. 61904070 and 51802129).

Notes and references

- J. Qi, W. Zhang and R. Cao, Solar-to-Hydrogen energy conversion based on water splitting, *Adv. Energy Mater.*, 2018, **8**, 1701620.
- J. Liang, X. Li, Z. Yu, G. Zeng, Y. Luo, L. Jiang, Z. Yang, Y. Qian and H. Wu, Amorphous MnO₂ modified biochar derived from aerobically composted swine manure for adsorption of Pb(II) and Cd(II), *ACS Sustainable Chem. Eng.*, 2017, **5**, 5049.
- L. Jiang, X. Yuan, Y. Pan, J. Liang, G. Zeng, Z. Wu and H. Wang, Doping of graphitic carbon nitride for photocatalysis: a review, *Appl. Catal., B*, 2017, **217**, 388.
- X. J. Wen, C. Niu, L. Zhang, C. Liang and G. Zeng, A novel Ag₂O/CeO₂ heterojunction photocatalysts for photocatalytic degradation of enrofloxacin: possible degradation pathways, mineralization activity and an in depth mechanism insight, *Appl. Catal., B*, 2018, **221**, 701.
- C. Zhou, C. Lai, D. Huang, G. Zeng, C. Zhang, M. Cheng, L. Hu, J. Wan, W. Xiong, M. Wen, X. Wen and L. Qin, Highly porous carbon nitride by supramolecular preassembly of monomers for photocatalytic removal of sulfamethazine under visible light driven, *Appl. Catal., B*, 2018, **220**, 202.
- M. Solakidou, A. Giannakas, Y. Georgiou, N. Boukos, M. Louloudi and Y. Deligiannakis, Efficient photocatalytic water-splitting performance by ternary CdS/Pt-N-TiO₂ and CdS/Pt-N,F-TiO₂: interplay between CdS photocorrosion and TiO₂-doping, *Appl. Catal., B*, 2019, **254**, 194.
- T. Yang, K. Xue, J. Wang, R. He, R. Sun, U. Omeoga, T. Yang, W. Wang, J. Wang and Y. Hu, Investigation of electron beam irradiation on In₂S₃-M_xIn_yS_z (M = Bi or La) Z-scheme heterojunctions for efficient and stable degradation of water pollutants, *J. Alloys Compd.*, 2020, **818**, 152873.
- V. Jayarama, B. Palanivel, C. Ayappan, M. Chellamuthu and A. Mani, CdZnS solid solution supported Ce₂Sn₂O₇ pyrochlore photocatalyst that proves to be an efficient candidate towards the removal of organic pollutants, *Sep. Purif. Technol.*, 2019, **224**, 405–420.
- E. Hua, S. Jin, X. Wang, S. Ni, G. Liu and X. Xu, Ultrathin 2D type-II p-n heterojunctions La₂Ti₂O₇/In₂S₃ with efficient charge separations and photocatalytic hydrogen evolution under visible light illumination, *Appl. Catal., B*, 2019, **245**, 733.
- J. Low, J. Yu, M. Jaroniec, S. Wageh and A. Al-Ghamdi, Heterojunction Photocatalysts, *Adv. Mater.*, 2017, **29**, 1601694.
- H. Wang, L. Zhang, Z. Chen, J. Hu, S. Li, Z. Wang, J. Liu and X. Wang, Semiconductor heterojunction photocatalysts: design, construction, and photocatalytic performances, *Chem. Soc. Rev.*, 2014, **43**, 5234.
- H. Yu, R. Shi, Y. Zhao, G. Waterhouse, L. Wu, C. Tung and T. Zhang, Smart Utilization of Carbon Dots in Semiconductor Photocatalysis, *Adv. Mater.*, 2016, **28**, 9454.
- Q. Li, X. Li, S. Wageh, A. Al-Ghamdi and J. Yu, CdS/Graphene Nanocomposite Photocatalysts, *Adv. Energy Mater.*, 2015, **5**, 1500010.
- X. Li, J. Yu and M. Jaroniec, Hierarchical photocatalysts, *Chem. Soc. Rev.*, 2016, **45**, 2603.
- H. Li, W. Tu, Y. Zhou and Z. Zou, Z-Scheme Photocatalytic Systems for Promoting Photocatalytic Performance: Recent Progress and Future Challenges, *Adv. Sci.*, 2016, **3**, 1500389.
- P. Zhou, J. Yu and M. Jaroniec, All-Solid-State Z-Scheme Photocatalytic Systems, *Adv. Mater.*, 2014, **26**, 4920.
- T. Pan, D. Chen, W. Xu, J. Fang, S. Wu, Z. Liu, K. Wu and Z. Fang, Anionic polyacrylamide-assisted construction of thin 2D-2D WO₃/g-C₃N₄ Step-scheme heterojunction for enhanced tetracycline degradation under visible light irradiation, *J. Hazard. Mater.*, 2020, **393**, 122366.
- M. Kim, Y. Kim, S. Lim, S. Kim and S. In, Efficient visible light-induced H₂ production by Au@CdS/TiO₂ nanofibers: synergistic effect of core-shell structured Au@CdS and densely packed TiO₂ nanoparticles, *Appl. Catal., B*, 2015, **166**, 423.
- X. Yin, J. Liu, W. Jiang, X. Zhang, J. Hu and L. Wan, Urchin-like Au@CdS/WO₃ micro/nano heterostructure as a visible-light driven photocatalyst for efficient hydrogen generation, *Chem. Commun.*, 2015, **51**, 13842.
- J. Wang, Y. Zhang, X. Wang and W. Su, Simultaneous enhancements in photoactivity and anti-photocorrosion of Z-scheme Mn_{0.25}Cd_{0.75}S/WO₃ for solar water splitting, *Appl. Catal., B*, 2020, **268**, 118444.
- J. Li, H. Cheng, Y. Chiu and Y. Hsu, ZnO-Au-SnO₂ Z-scheme photoanodes for remarkable photoelectrochemical water splitting, *Nanoscale*, 2016, **8**, 15720.
- X. Wen, C. Niu, L. Zhang, C. Liang, H. Guo and G. Zeng, Photocatalytic degradation of ciprofloxacin by a novel Z-scheme CeO₂-Ag/AgBr photocatalyst: influencing factors, possible degradation pathways, and mechanism insight, *J. Catal.*, 2018, **358**, 141.
- H. Li, Y. Gao, Y. Zhou, F. Fan, Q. Han, Q. Xu, X. Wang, M. Xiao, C. Li and Z. Zou, Construction and Nanoscale Detection of Interfacial Charge Transfer of Elegant Z-Scheme WO₃/Au/In₂S₃ Nanowire Arrays, *Nano Lett.*, 2016, **16**, 5547.
- S. Bao, Q. Wu, S. Chang, B. Tian and J. Zhang, Z-scheme CdS-Au-BiVO₄ with enhanced photocatalytic activity for organic contaminant decomposition, *Catal. Sci. Technol.*, 2017, **1**(7), 124–132.
- J. Jiang, Y. Song, X. Wang, T. Li, M. Li, Y. Lin, T. Xie and S. Dong, Enhancing aqueous pollutant photodegradation via a Fermi level matched Z-scheme BiOI/Pt/g-C₃N₄ photocatalyst: unobstructed photogenerated charge behavior and degradation pathway exploration, *Catal. Sci. Technol.*, 2020, **10**, 3324.
- J. Zhang, Y. Ma, Y. Du, H. Jiang, D. Zhou and S. Dong, Carbon nanodots/WO₃ nanorods Z-scheme composites:



- Remarkably enhanced photocatalytic performance under broad spectrum, *Appl. Catal., B*, 2017, **209**, 253.
- 27 X. Yuan, L. Jiang, J. Liang, Y. Pan, J. Zhang, H. Wang, L. Leng, Z. Wu, R. Guan and G. Zeng, In situ synthesis of 3D microsphere-like $\text{In}_2\text{S}_3/\text{InVO}_4$ heterojunction with efficient photocatalytic activity for tetracycline degradation under visible light irradiation, *Chem. Eng. J.*, 2019, **356**, 371.
 - 28 T. Yan, T. Wu, Y. Zhang, M. Sun, X. Wang, Q. Wei and B. Du, Fabrication of $\text{In}_2\text{S}_3/\text{Zn}_2\text{GeO}_4$ composite photocatalyst for degradation of acetaminophen under visible light, *J. Colloid Interface Sci.*, 2017, **506**, 197.
 - 29 Z. Li, Z. Zhou, J. Ma, Y. Li, W. Peng, G. Zhang, F. Zhang and X. Fan, Hierarchical photocatalyst of In_2S_3 on exfoliated MoS_2 nanosheets for enhanced visible-light-driven Aza-Henry reaction, *Appl. Catal., B*, 2018, **237**, 288.
 - 30 H. Xu, Y. Wang, X. Dong, N. Zheng, H. Ma and X. Zhang, Fabrication of $\text{In}_2\text{O}_3/\text{In}_2\text{S}_3$ microsphere heterostructures for efficient and stable photocatalytic nitrogen fixation, *Appl. Catal., B*, 2019, **257**, 117932.
 - 31 L. Zhang, S. Li, B. Liu, D. Wang and T. Xie, Highly Efficient CdS/WO_3 Photocatalysts: Z-Scheme Photocatalytic Mechanism for Their Enhanced Photocatalytic H_2 Evolution under Visible light, *ACS Catal.*, 2014, **4**, 3724.
 - 32 B. Li, L. Sun, J. Bian, N. Sun, J. Sun, L. Chen, Z. Li and L. Jing, Controlled synthesis of novel Z-scheme iron phthalocyanine/porous WO_3 nanocomposites as efficient photocatalysts for CO_2 reduction, *Appl. Catal., B*, 2020, **270**, 118849.
 - 33 N. Omrani and A. Nezamzadeh-Ejhi, A comprehensive study on the enhanced photocatalytic activity of $\text{Cu}_2\text{O}/\text{BiVO}_4/\text{WO}_3$ nanoparticles, *J. Photochem. Photobiol., A*, 2020, **389**, 112223.
 - 34 Q. Qiu, S. Li, J. Jiang, D. Wang, Y. Lin and T. Xie, Improved Electron Transfer between TiO_2 and FTO Interface by N-Doped Anatase TiO_2 Nanowires and Its Applications in Quantum Dot-Sensitized Solar Cells, *J. Phys. Chem. C*, 2017, **121**, 21560.
 - 35 X. Wei, T. Xie, Y. Zhang, D. Wang and J. Chen, The Effect of Al^{3+} Treatment on Charge Dynamics in Dye-sensitized Nanocrystal-line TiO_2 Solar Cells Explored by Photovoltage Measurements, *Mater. Chem. Phys.*, 2010, **122**, 259.
 - 36 J. Jiang, H. Wang, X. Chen, S. Li, T. Xie, D. Wang and Y. Lin, Enhanced photocatalytic degradation of phenol and photogenerated charges transfer property over BiOI -loaded ZnO composites, *J. Colloid Interface Sci.*, 2017, **494**, 130.
 - 37 L. Zhang, T. Jiang, S. Li, Y. Lu, L. Wang, X. Zhang, D. Wang and T. Xie, Enhancement of Photocatalytic H_2 Evolution on $\text{Zn}_{0.8}\text{Cd}_{0.2}\text{S}$ Loaded with CuS as Cocatalyst and its Photogenerated Charge Transfer Properties, *Dalton Trans.*, 2013, **42**, 12998.
 - 38 Y. Zhang, J. Yu, M. Jaroniec and J. Gong, Noble Metal-Free Reduced Graphene Oxide- $\text{Zn}_x\text{Cd}_{1-x}\text{S}$ Nanocomposite with Enhanced Solar Photocatalytic H_2 -Production Performance, *Nano Lett.*, 2012, **12**, 4584.
 - 39 Y. Ma, J. Jiang, A. Zhu, P. Tan, Y. Bian, W. Zeng, H. Cui and J. Pan, Enhanced visible-light photocatalytic degradation by $\text{Mn}_3\text{O}_4/\text{CeO}_2$ heterojunction: a Z-scheme system photocatalyst, *Inorg. Chem. Front.*, 2018, **5**, 2579.
 - 40 B. He, M. Feng, X. Chen, D. Zhao and J. Sun, One-pot construction of chitin-derived carbon/g- C_3N_4 heterojunction for the improvement of visible-light photocatalysis, *Appl. Surf. Sci.*, 2020, **527**, 146737.
 - 41 C. Yao, X. Wang, W. Zhao, T. Li, Y. He, X. Ran and L. Guo, Probing the facet-dependent intermediate in the visible-light degradation of RhB by carbon-coated anatase TiO_2 nanoparticles, *J. Alloys Compd.*, 2020, **846**, 156335.
 - 42 B. Song, Q. Wang, L. Wang, J. Lin, X. Wei, V. Murugadoss, S. Wu, Z. Guo, T. Ding and S. Wei, Carbon nitride nanoplatelet photocatalysts heterostructured with B-doped carbon nanodots for enhanced photodegradation of organic pollutants, *J. Colloid Interface Sci.*, 2020, **559**, 124.
 - 43 G. Ma, J. Lu, Q. Meng, H. Lv, L. Shui, Y. Zhang, M. Jin, Z. Chen, M. Yuan, R. Nötzel, X. Wang, C. Wang, J. Liu and G. Zhou, Synergistic effect of Cu-ion and WO_3 nanofibers on the enhanced photocatalytic degradation of Rhodamine B and aniline solution, *Appl. Surf. Sci.*, 2019, **451**, 306.
 - 44 X. Yuan, L. Jiang, X. Chen, L. Leng, W. Hou, Z. Wu, T. Xiong, J. Liang and G. Zeng, Highly efficient visible-light-induced photoactivity of Z-scheme $\text{Ag}_2\text{CO}_3/\text{Ag}/\text{WO}_3$ photocatalysts for organic pollutant degradation, *Environ. Sci.: Nano*, 2017, **4**, 2175.
 - 45 X. Gao, C. Liang, K. Gao, X. Li, J. Liu and Q. Li, Z-scheme heterojunction $\text{Ag}_3\text{PO}_4/\text{BiVO}_4$ with exposing high-active facets and stretching spatial charge separation ability for photocatalytic organic pollutants degradation, *Appl. Surf. Sci.*, 2020, **524**, 146506.
 - 46 Z. Shi, Y. Zhang, T. Liu, W. Cao, L. Zhang, M. Li and Z. Chen, Synthesis of $\text{BiOBr}/\text{Ag}_3\text{PO}_4$ heterojunctions on carbon-fiber cloth as filter-membrane-shaped photocatalyst for treating the flowing antibiotic wastewater, *J. Colloid Interface Sci.*, 2020, **575**, 183.
 - 47 H. Yin, Y. Cao, T. Fan, B. Qiu, M. Zhang, J. Yao, P. Li, X. Liu and S. Chen, Construction of carbon bridged TiO_2/CdS tandem Z-scheme heterojunctions toward efficient photocatalytic antibiotic degradation and Cr (VI) reduction, *J. Alloys Compd.*, 2020, **824**, 153915.
 - 48 S. Li, Q. Zhao, D. Meng, D. Wang and T. Xie, Fabrication of metallic charge transfer channel between photoanode $\text{Ti}/\text{Fe}_2\text{O}_3$ and cocatalyst CoOx : an effective strategy for promoting photoelectrochemical water oxidation, *J. Mater. Chem. A*, 2016, **4**, 16661.
 - 49 X. Wei, T. Xie, D. Xu, Q. Zhao, S. Pang and D. Wang, A study of the dynamic properties of photo-induced charge carriers at nanoporous TiO_2 /conductive substrate interfaces by the transient photovoltage technique, *Nanotechnology*, 2008, **27**, 275707.
 - 50 Y. Zhang, T. Xie, T. Jiang, X. Wei, S. Pang, X. Wang and D. Wang, Surface photovoltage characterization of a ZnO nanowire array/ CdS quantum dot heterogeneous film and its application for photovoltaic devices, *Nanotechnology*, 2010, **23**, 7217.

